

RESEARCH ARTICLE

10.1002/2015JA021443

Resolute Bay Incoherent Scatter Radar observations of plasma structures in the vicinity of polar holes

Key Points:

- Density depressions in the polar cap show no preference toward either slow or fast convection
- Polar holes can be in part refilled by series of polar patches propagating from dayside
- Mesoscale density structures are elongated and drift with plasma convection velocity

Correspondence to:

R. A. Makarevich,
rmakarevich@alaska.edu

Citation:

Makarevich, R. A., L. J. Lamarche, and M. J. Nicolls (2015), Resolute Bay Incoherent Scatter Radar observations of plasma structures in the vicinity of polar holes, *J. Geophys. Res. Space Physics*, 120, 7970–7986, doi:10.1002/2015JA021443.

Received 8 MAY 2015

Accepted 19 AUG 2015

Accepted article online 24 AUG 2015

Published online 18 SEP 2015

Roman A. Makarevich¹, L. J. Lamarche¹, and M. J. Nicolls²

¹Geophysical Institute and Department of Physics, University of Alaska Fairbanks, Fairbanks, Alaska, USA, ²Center for Geospace Studies, SRI International, Menlo Park California, USA

Abstract The Resolute Bay Incoherent Scatter Radar North (RISR-N) data collected between January 2012 and June 2013 are employed to identify and analyze 14 events with significant plasma density depressions ($N_e < 4 \times 10^{10} \text{ m}^{-3}$) in the winter polar cap ionosphere. The RISR-N observations near a magnetic latitude (MLAT) of 85°N refer to the region poleward of the previously identified polar hole-auroral cavity region $70^\circ\text{--}80^\circ\text{ MLAT}$ where extremely low densities (down to $2 \times 10^8 \text{ m}^{-3}$ near 300 km in altitude) are found at times. Multipoint observations by RISR-N are also characterized by multiple series of propagating local density enhancements (plasma structures) both well outside and in the vicinity of polar holes. A superposed epoch analysis of plasma density and convection reveals that the density depressions tend to reach their minimum near the reversal of the meridional convection component. The wavelet analysis of plasma density time series shows that the wave power is enhanced within the depressions and tends to peak near the density minimum. The plasma structures are more elongated at mesoscales ($>150 \text{ km}$), with no apparent differences between structure shapes outside and inside low-density regions. The structure propagation velocity is perpendicular to its elongation direction and consistent with that of the large-scale plasma convection. The observations indicate that large-scale density depressions can form under a variety of convection conditions and that plasma structuring processes outside the depressions may be responsible for their partial filling.

1. Introduction

The current view of the polar cap ionosphere is that of a highly structured region, with plasma density structures ranging in size between 10 m and 1000 km under both daytime and nighttime conditions (see recent review by Carlson [2012]). The plasma density is enhanced within patches, blobs, arcs, and tongues, while holes and cavities are fittingly characterized by lower densities as compared with background plasma.

The plasma density can be depressed particularly strongly just poleward of the statistical auroral oval within the regions termed polar holes [Brinton *et al.*, 1978] and auroral cavities [Doe *et al.*, 1993]. These extremely low densities (down to 200 cm^{-3} near 300 km in altitude) are typically found in the dawn *F* region between 70° and 80° magnetic latitude (MLAT) when solar activity is low [Hoegy and Grebowsky, 1991]. Polar holes and auroral cavities have been identified using different observational techniques, but they are statistically collocated so that a common term of the polar hole-auroral cavity region, or simply *the polar hole*, has been used more recently [Benson and Grebowsky, 2001]. It is thought that a polar hole can form either due to continuous recombination over a long interval under quiet conditions [Sojka *et al.*, 1981a, 1981b] or large downward plasma transport driven by strong convection [Sojka *et al.*, 1981c].

Localized enhancements in plasma density (100–1000 km in extent) known as polar patches have received even more attention than their low-density counterparts [Buchau *et al.*, 1983; Weber *et al.*, 1984; Rodger *et al.*, 1994; Milan *et al.*, 2002; Hosokawa *et al.*, 2009; Dahlgren *et al.*, 2012a, 2012b; Zhang *et al.*, 2013; Burston *et al.*, 2014; Goodwin *et al.*, 2015]. A fundamental problem is what causes the plasma to be chopped into islands and what happens with patches after they have been separated from their source region including further structuring processes [Carlson, 2012].

In many ways, polar holes and patches represent two opposite sides of the same structured polar cap system, without being directly related to each other. Significant internal structure was found to be common, however, to both polar holes [Crowley *et al.*, 1993] and patches [Carlson *et al.*, 2007; Hosokawa *et al.*, 2009; Moen *et al.*,

2012; Oksavik et al., 2012]. The nature of this internal structure is well understood for patches [Carlson, 2012], but less so for polar holes, with few reported observations at such small scales [Crowley et al., 1993]. Moreover, mesoscale plasma density enhancements, i.e., with sizes smaller than the typical extent of the polar hole but larger than those of irregularities producing scintillation and coherent backscatter, may also represent the internal structure of the polar hole. It is largely unknown, however, whether such plasma enhancements can be generated inside the polar hole or propagate into the polar hole from outside and whether a polar hole can, in part or fully, be refilled by these plasma enhancements.

The other common theme between polar holes and patches is the critical role of the high-latitude plasma convection in their formation and evolution. Slow convection is believed to be responsible for generation of quiet-time polar holes [Sojka et al., 1981a], while polar patches are expected to drift with the background plasma antisunward across the polar cap and possibly even continue with the return flow in the dawn and dusk sectors [Moen et al., 2007; Oksavik et al., 2010; Zhang et al., 2015]. One challenge in that regard is the need to track individual structures continuously and measure their propagation velocity \mathbf{V}_{str} while simultaneously measuring the background convection velocity $\mathbf{V}_{E \times B}$. While agreement between \mathbf{V}_{str} and $\mathbf{V}_{E \times B}$ is widely expected for polar patches, particularly deep in the polar cap region, experimental comparisons were mostly limited to case studies based on radar observations [Oksavik et al., 2010; Bahcivan et al., 2010]. Similarly, it has not yet been experimentally established where, in relation to the convection pattern, polar holes occur, reach their minimum density, and start to decay.

The issue that is important for both estimating the propagation velocity of plasma structures and identifying their possible origins is analysis of structure shapes and elongation directions. Most polar patches are expected to be cigar shaped and elongated in the east-west (EW) direction, assuming that the dayside magnetic reconnection is a predominant production mechanism [Lockwood and Carlson, 1992; Carlson, 2003]. Several examples of such patches have been presented recently, and their EW extent has been estimated to be 1500–2000 km using dual airglow imager observations [Hosokawa et al., 2014]. Further analysis is needed in order to ascertain whether all or most structures are cigar shaped rather than circular, particularly with smaller-scale patches. If most structures are indeed cigar shaped, the other related issue may become important, namely, whether structures have a significant propagation velocity component in the direction of elongation. This is because inferring the structure propagation velocity \mathbf{V}_{str} from latitude-time, range-time, or other keogram-like plots can only provide the apparent velocity from which the elongation-perpendicular component can be determined if appropriate corrections are applied [e.g., Makarevitch et al., 2004]. This is usually not an issue if the structure is more circular and/or if the extent is smaller than the instrument's field of view (FoV).

The deployment of the northward looking face of the Resolute Bay Incoherent Scatter Radar North (RISR-N) in 2009 and the large accumulated data set of direct electron density measurements provide an excellent opportunity to further investigate polar cap density structures. The important advantages of using RISR-N in addressing the above discussed issues include (a) good coverage of the solar cycle minimum where polar holes are typically found, (b) multipoint nature of RISR-N measurements with ability to image, track, and estimate the propagation velocity of small-scale and mesoscale density structures \mathbf{V}_{str} , and (c) concurrent direct measurements of the plasma convection velocity $\mathbf{V}_{E \times B}$. The specific objectives of this study are (1) to establish where significant density depletions occur in relation to the background plasma convection, (2) to investigate a possible role of small-scale and mesoscale density enhancements in refilling of polar holes, and (3) to quantify density structures in terms of their shape, direction of elongation, and propagation velocity and to analyze differences between small-scale and mesoscale structures.

2. Experiment Configuration and Data Analysis

The electron density data set employed in this study comprised the data from the RISR-N system located in Resolute Bay, Canada (74.7°N, 94.9°W, MLAT = 82.7°N) [Bahcivan et al., 2010]. RISR-N is a phased-array system with a narrow beam that can be steered electronically in many directions within the viewing area. Data from multiple beams can be collected nearly simultaneously (sequentially on a pulse-by-pulse basis but with a very high time cadence) within the same integration period. RISR-N has been in routine operation since August 2009, and the current study considered the data collected between January 2012 and June 2013. This was the period with the most recent processed data obtained using a common series of World Day modes (see below). The time resolution throughout this period was ~ 1 min.

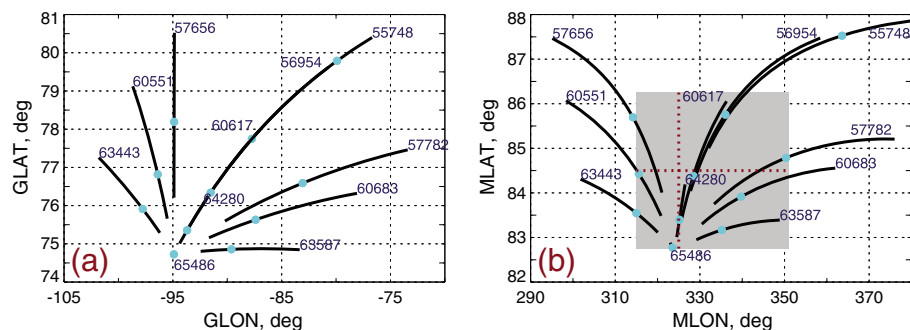


Figure 1. RISR-N experiment configuration in the WorldDay64m mode in (a) geographic and (b) geomagnetic coordinates. Shown are 11 beams corresponding to the long pulse (LP) data. The start of the gate nearest to a 300 km altitude is shown by a blue circle for each beam. The standard RISR-N beam identification is also given by the digits near the maximum altitude coordinates. The grey-shaded rectangle in Figure 1b shows the area included in density interpolations. The dark red dotted lines within the grey rectangle show MLAT and MLON of keograms considered.

RISR-N modes use two sets of interleaved pulses: a long pulse (LP) with 72 km range resolution designed for F region studies and an alternating code pulse with 4.5 km resolution used for E region studies. The data on the electron density, ion and electron temperatures, and ion drift velocity are obtained from the measured power spectra using a standard incoherent scatter radar (ISR) technique involving iterative nonlinear least squares fitting and calibration [Evans, 1969; Rishbeth and Williams, 1985; Nicolls et al., 2007]. The RISR-N calibration involves plasma line measurements during summer daytime periods or ionosonde measurements at Resolute during other periods [Bahcivan et al., 2010; Themens et al., 2014]. The noise and system constants are estimated and accounted for during the calibration process [Nicolls et al., 2007]. Uncertainties in the fitted parameters are estimated using their known relationships with the uncertainty in the signal power $\Delta P_s/P_s$, which depends on the signal-to-noise ratio (SNR), bandwidth b , pulse width τ , repetition frequency n , and observing time t as $(1 + \text{SNR}^{-1}) / (bn\tau t)^{1/2}$ [Rishbeth and Williams, 1985]. The choice of operational parameters is such that uncertainties of less than 10% are obtained for SNRs as small as 0.16 ($\text{SNR}^{-0.5} = 2.5$) [Davis and McCrea, 2004, Figure 1].

RISR-N is typically scheduled to run for 5–6 days per month in a common mode WorldDay. Technical specification such as beam number and orientations, pulse sequences, and cadence period change slightly from one WorldDay mode to another in response to experimental demands and prior results. The current study employed the data collected in two such modes: WorldDay64m (January to November 2012) and WorldDay66m (December 2012 to June 2013). Other (special) modes are also run but were not considered here to keep the data set as uniform as possible. In both WorldDay modes considered, the data were collected in 11 beams. Figure 1 shows (a) geographic and (b) geomagnetic coordinates sampled by these beams in the WorldDay64m mode. The beams range from vertical (and approximately magnetic field aligned at these MLATs) beam 65486 to the highly inclined meridional beam 55748 (geographic azimuth of 26° and elevation of 20°).

In this study, we employed the LP data for the electron density near 300 km in altitude. The radar gates closest to this altitude are shown by blue circles in Figure 1. The exact altitudes of these gates changed slightly from one beam to another, but the average difference from 300 km in altitude was only 7.2 km. At this altitude, the 11 beams cover well an area extending $315^\circ - 350^\circ\text{E}$, $82.75^\circ - 86.25^\circ\text{N}$ in geomagnetic coordinates. This area is shown by the grey rectangle in Figure 1b. These limits were also used in producing interpolated 2-D images of electron density at 300 km and keograms based on them (see examples in section 3). The bin sizes used in interpolation were 0.25° in MLAT and 1° in magnetic longitude (MLON). The limits were chosen so that the interpolated images would represent well the raw density data in all beams (i.e., minimal spurious features and artifacts of interpolation). This was very much the case (see examples in section 3.2), particularly at MLON and MLAT at which density keograms were considered (red dashed lines within the grey area in Figure 1b). Similar analysis is implemented on a routine basis in many other ground-based techniques that use multiple beams, e.g., imaging riometry [e.g., Kellerman and Makarevich, 2011]. All 11 beams have contributed to these images, but their contribution varied depending on the closeness to the point of interest. The top edge in MLAT was chosen to be somewhat higher than the two gates at $\sim 85.75^\circ\text{N}$ (blue circles in Figure 1b) to keep both MLON and MLAT extents close to 400 km and minimize biases related to different MLON and MLAT extents.

The standard plasma convection data corrected for the neutral motions were also employed. These estimates were obtained from the line-of-sight (LOS) ion velocity LP data using a method described by *Heinselman and Nicolls* [2008]. In this method, the 3-D convection electric field vectors \mathbf{E} are obtained from the ion drift LOS components in LP gates above 150 km in altitude. All LOS components are combined within a particular MLAT bin to produce a single \mathbf{E} estimate with a full error covariance estimate. The two major assumptions imposed on the data in the form of a given covariance matrix are (1) flow uniformity within each MLAT bin and (2) negligible vertical winds. The \mathbf{E} estimates obtained under these assumptions are also converted to the convection velocities which are resolved into the east-west (V_{east}) and north-south (V_{nor}) field-perpendicular components in magnetic coordinates; most of the analysis below used these components as well as field-perpendicular 2-D velocity vectors $\mathbf{V}_{\mathbf{E} \times \mathbf{B}}$. Since in the standard method only variation in MLAT (but not MLON) is considered, measurements are assigned to a MLON near the central meridian of the FoV. In the following analysis, this MLON is chosen to be the same as a MLON of the north-south (NS) density keograms (325°E).

This analysis focused on the density measurements near 300 km in altitude, similar to previous studies of the polar holes [e.g., *Crowley et al.*, 1993]. Daily time series of density at (325°E, 84.5°N, magnetic) were considered, and days were selected that had at least 1% of measurements with $N_e < 4 \times 10^{10} \text{ m}^{-3}$ and at least 10% of measurements with $N_e < 10^{11} \text{ m}^{-3}$. These density threshold values are somewhat higher than densities reported within the deepest polar holes (see a detailed discussion of this issue in section 4.1), but this particular choice resulted in a reasonable number of events that all showed deep density depressions as compared with daytime observations during the same events.

In total, 14 days satisfied these criteria between January 2012 and June 2013, with all of them occurring in the winter period (October–February). These 14 events in the YYYYMMDD format were 20120115, 20120219, 20121008, 20121013, 20121104, 20121105, 20121111, 20121112, 20121211, 20121212, 20121213, 20121214, 20130212, and 20130223. In the following section, we present some representative examples of these events and several statistical analyses involving all 14 events. The total number of single-point measurements was 18,251.

3. Observations

3.1. Electron Density Measurements and Model

Analysis of strong density depletions measured by RISR-N in the context of the International Reference Ionosphere (IRI) 2007 model [*Bilitza and Reinisch*, 2008] is useful in identifying the extent to which the density deviates from the expected trend. The exact or even approximate agreement is not necessarily expected since polar holes may be regarded as the regions where some of the strongest negative perturbations from the expected trend occur.

Figure 2 shows (a) the line and (b) scatterplots of RISR-N and IRI densities on 12 February 2013. Out of all 14 days, this was the day with the strongest agreement as expressed in the linear correlation coefficient r of 0.828. On other days, the coefficients ranged between 0.33 and 0.80, with the average being 0.61. The density values shown are for the range gate nearest to a 300 km altitude in beam 64280, which refers to geographic coordinates of 75.35°N, 93.68°W. Strong negative deviation from the IRI trend is evident between 02 and 14 UT. This refers to nighttime observations at 19–05 magnetic local time (MLT) since $\text{MLT} \approx \text{UT} - 7\text{h}$ for RISR-N. For this event, the density uncertainties are shown by the vertical green lines. The fact that the measured densities at 02–14 UT were below the IRI trend within uncertainty for all density values means that the differences were significant.

Figures 2c and 2d show the same comparison but for all 14 events. Here the dark grey line (light grey stripe) is the average values (mean ± 1 standard deviation) for the binned density for all RISR-N data collected during the winter between January 2012 and February 2013. These values represent the “normal” density range in winter according to RISR-N measurements. The blue circles and bars present the same information but only for 14 selected events. Finally, the orange histogram at the bottom of Figure 2c shows the fraction of points (for 14 events only) below the normal range within their individual uncertainties. These individual uncertainties are not shown in Figures 2c and 2d to keep the diagram readable, but they were very similar to uncertainties given by the green lines in Figures 2a and 2b. The scale for the fraction values is given by the three tick values on the right of Figure 2c, with the maximum value of 28.3% at 03–04 UT just below the tick value of 30%.

From Figure 2c, low densities are generally observed at 02–12 UT (19–05 MLT), with the binned data (blue circles and bars) being below IRI trends (red lines) at 06–11 UT (23–04 MLT) within uncertainty. Interestingly

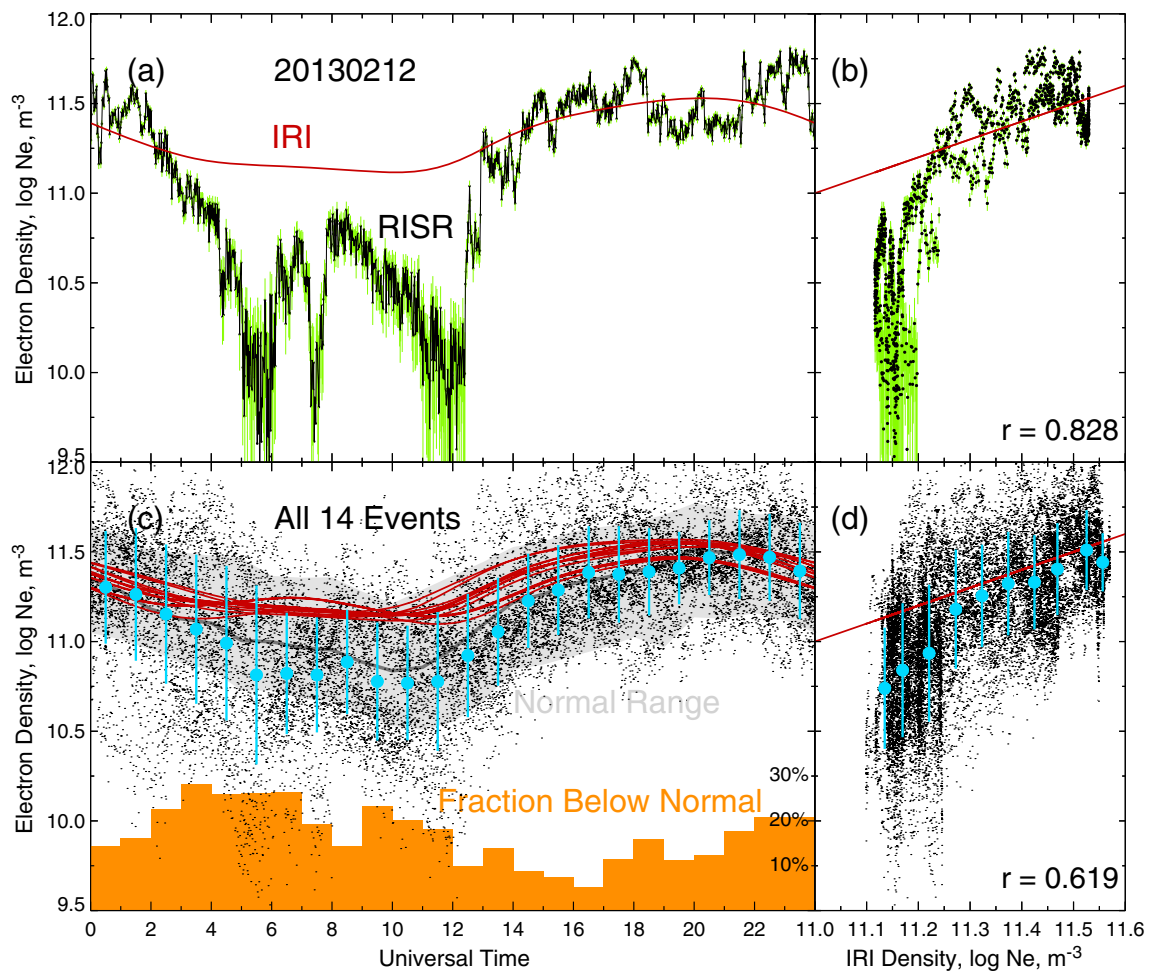


Figure 2. Comparison of the IRI model and RISR-N measured electron densities at 308 km altitude at coordinates 75.35°N, 93.68°W (geographic) or 83.40°N, 325.16°E (geomagnetic). The RISR-N density is plotted versus (a) UT and (b) IRI density for 12 February 2013. Uncertainties in the measured density are shown by the vertical green lines. In both panels, points on the red line represent perfect agreement with IRI. (c and d) The same comparison but for all 14 events considered. The grey line and stripe in Figure 2c show the binned RISR-N density in 1h bins obtained from all available winter measurements (October–February) between January 2012 and February 2013, while blue circles and bars show the binned data from the 14 considered events. The orange histogram shows the fraction of measurements in each 1h bin that was below the normal density range (grey stripe), with the scale given by the three tick values (10%, 20%, and 30%) on the right of Figure 2c. Linear correlation coefficients r between the IRI and RISR-N densities are given in Figures 2b and 2d.

though, it is not just the 14 events that show significant deviations from IRI trends but also most other winter days according to the “normal range” information. Thus, the IRI trends are within one standard deviation (grey stripe) but only just, being quite close to the top of this range. The fraction of points that are below this normal range (orange histogram) shows an increase at 02 UT and a drop after 12 UT. Interestingly, there is another drop at 07–09 UT, which is also reflected in the relative absence of low-density measurements (black dots) at this time. The same feature can be seen in the binned values (blue circles) that also show a peak at 08 UT. This implies that a secondary density peak observed near 08 UT for the event shown in Figure 2a could be a repeating feature, at least for a significant subset of events.

The point-by-point comparison plots of Figures 2b and 2d show that densities generally agree for high values of $\log N_e > 11.3$, as evident from the blue binned values being close to the red line of ideal coincidence. However, RISR-N densities are generally much lower than their IRI counterparts at low values of $\log N_e < 11.3$ since most black dots are below the red line within uncertainty at these values. The smallest binned value is below the red line of ideal coincidence within uncertainty, and the next two blue bars overlap with the red line but only just. Overall, Figure 2 demonstrates that the measured densities during low-density events are much lower than the expected trends and that this feature is not necessarily restricted to days when densities are particularly depressed.

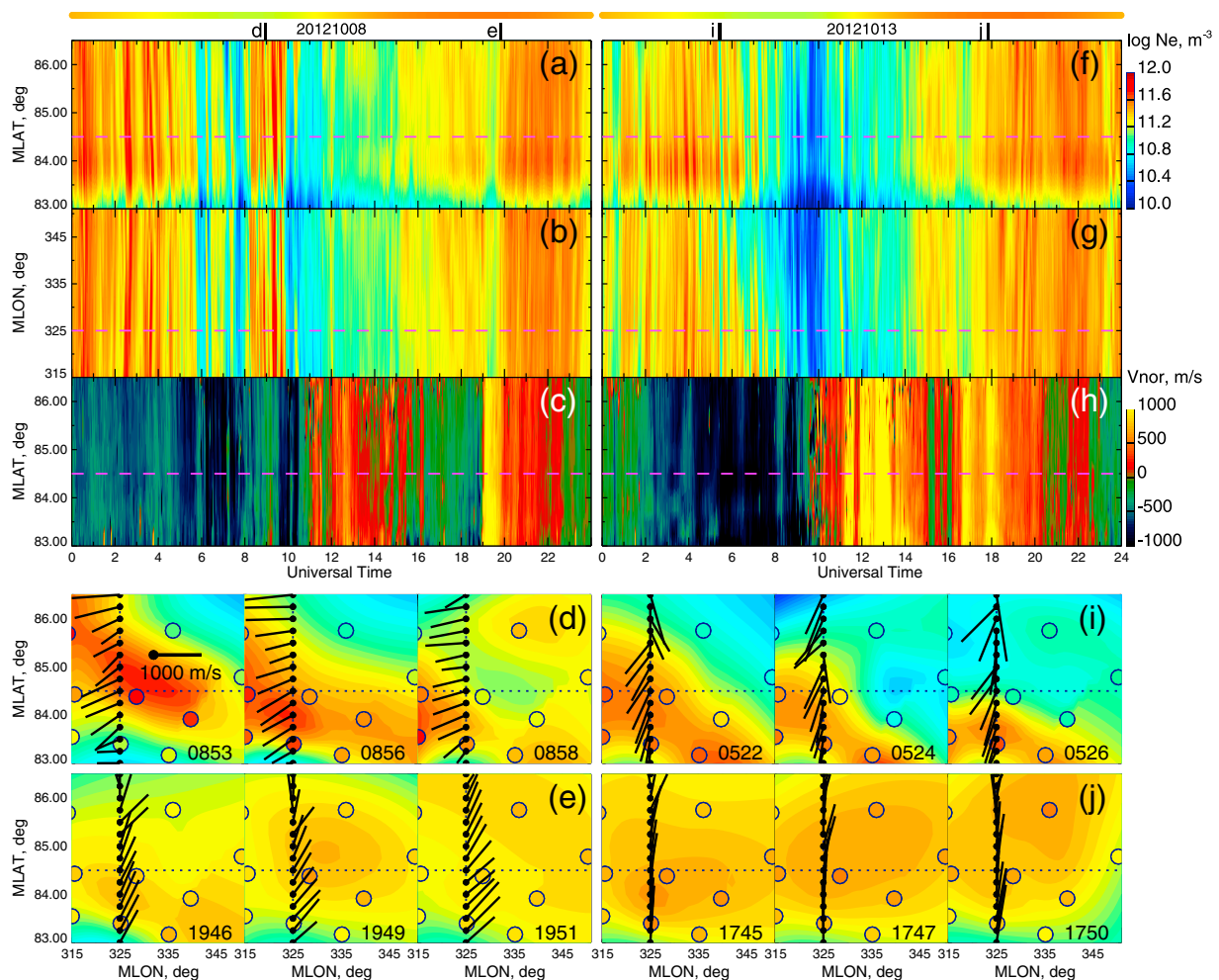


Figure 3. Keograms of (a) electron density at 325°E in MLON and 300 km in altitude, (b) electron density at 84.5°N in MLAT, and (c) NS convection velocity component on 8 October 2012. (d and e) Selected sequences of 2-D density images. The start time of each frame in UT (in HHMM format) is shown in the bottom right corner of each image. The density measured in each of the 11 beams at 300 km is shown by large colored circles. Black vectors show convection velocity vectors for each frame. The vector scale is given in Figure 3d. The small vertical lines and letters at the top of Figure 3a show the two selected intervals (d) and (e). The color scale is the same for Figures 3a, 3b, 3d, and 3e and is given to the right of Figure 3f. (f–j) The same but for 13 October 2012. The IRI densities are shown to the top of each column using the same density color scale.

3.2. Density Structures and Plasma Convection

The density data in all 11 beams and for all 14 events were processed to produce 2-D density images from which density keograms at 325°E in MLON and at 84.5°N in MLAT were produced. The standard convection products V_{east} and V_{nor} are also available for each of the 0.25° bins in MLAT and for each time frame from which MLAT-versus-UT keograms are easily produced. Figures 3a–3c present an example of RISR-N observations in the form of daily (a) NS or MLAT keogram of density N_e , (b) EW or MLON keogram of N_e , and (c) NS or MLAT keogram of V_{nor} for one event on 8 October 2012. The corresponding IRI density daily series from Figure 2 is shown as the heavy line to the top of Figure 3a using the same color scale. Figures 3d and 3e present 2-D density images corresponding to two selected time intervals on that day. Every other image is shown in each of two 3-frame sequences (d) or (e). The time interval for all three frames is shown at the top of Figure 3a for both intervals. In addition, each image shows 2-D convection vectors \mathbf{V}_{ExB} assigned to a MLON of a NS keogram. Figures 3f–3j present the same information but for the next event on 13 October 2012.

The lowest densities (blue colors) in Figures 3a, 3b, 3f, and 3g are significantly lower than the IRI densities shown to the top of each column; this is the same feature as that seen in Figure 2. Significant small-scale variability is also evident in the measured plasma density, particularly in comparison with the smooth IRI trends. These perturbations are seen most clearly as series of propagating density enhancements with peak densities

of 11.2–11.6 in logarithmic scale (yellow to red colors). From hereinafter, these plasma density enhancements are referred to as “plasma structures” or simply “structures.” Several series of such structures are particularly clear in the first half of the first event and throughout most of the second event. The density enhancements are particularly strong at 08–10 UT or near interval (d) in the first event, where they exist on a relatively weak density background (blue colors). Another weaker series of structures is visible near 07 UT, and if it was not for these two series the period 06–12 UT would have more uniform and low density. In other words, it would be more similar to what is seen in the second event, where the density exhibits a deep minimum near 10 UT in Figure 3f. This low-density region is reasonably symmetric and also has short-lived enhancements, although the quasiperiodic nature of enhancements is less clear. The “main” series in the first event is observed at 08–10 UT, i.e., at about the same time as the main minimum in the second event (10 UT). Combined with strong similarities in overall density trends for both events including for the lowest observed densities in any given 2h period, this prompts an interpretation of the main series of density enhancements as the one that partly filled the hole in the first event. Another interesting feature is that small-scale variability is present in both density and convection data. For example, propagating structures are evident at 15–16 UT on 13 October 2012 in both Figures 3f and 3h.

For both events, the meridional propagation direction appears to be mostly south (north) in the first (second) half of the day, while zonal propagation is east (west) near 00 (12) UT. Figures 3c and 3h show that for the NS component this is consistent with the plasma velocity measurements. The measured EW component is not presented here for brevity, but it was also consistent with the structure propagation. This is further illustrated by the four sequences of 2-D density images in Figures 3d, 3e, 3i, and 3j. In the two sequences (d) and (i), the region of enhanced density steadily moves SW, which is also the convection direction according to convection vectors shown by the black vectors. In the bottom row sequences (e) and (j), the opposite structure drift and convection directions are observed (i.e., NE), although in the last case (j) the direction is more toward north. The density structures are stronger and more elongated in intervals (d) and (i), as compared with those in intervals (e) and (j). In terms of the extent to which the interpolated data represent the raw data in individual beams, it is reasonably good. For example, the density is elevated in the three beams near 85°N in MLAT in the first frame at 0853 UT in Figure 3d, while in the next frame at 0856 UT it is elevated in the six beams below 85°N, which is reflected in the 2-D structure moving down in MLAT.

All 14 events are included in the next analysis presented in Figure 4. Figures 4a–4c show a superposed epoch analysis (SEA) of (a) the NS keogram of density N_e , (b) the EW keogram of N_e , and (c) the NS keogram of V_{nor} . The zero epoch time was selected to be the main density minimum for each event (i.e., the time when the lowest density was observed over the entire event). The bottom two rows show a SEA of wave power of (d) N_e and (e) V_{nor} . This was obtained from the wavelet analysis of the N_e and V_{nor} time series at the MLAT/MLON value used for the keograms for each event. Figures 4f–4j show the same analysis but for zero epoch chosen to be the V_{nor} reversal.

Figures 4a and 4b show a deep depression in the electron density, with a somewhat steeper trailing edge. Comparing Figures 4a and 4b with Figure 4c, the density minimum coincides with the average V_{nor} changing from negative values around –300 m/s to highly variable (00–03h) and then mostly positive (03–12h) values. A similar analysis conducted for V_{east} did not show any distinct features in the SEA of the zonal convection component (not presented here), with the westward convection observed for ~6h on either side of zero epoch (i.e., inside, in the vicinity, and well outside of the density depression).

The feature of highly variable convection in the density depression is present even in the heavily averaged values of Figure 4c. When this variability is assessed first for each event (as represented by wavelet analysis) and only then followed by the SEA to bring up the typical features (Figures 4d and 4e), the variability becomes even clearer. The small-scale density variations peak in wave power within the density depression (pink line in Figure 4d), at least for the periods near 480s. The wave power for V_{nor} (Figure 4e) peaks right at the density minimum and across a wide range of periods (white area is extended vertically near zero epoch).

Overall, Figures 4a–4e demonstrate that the trailing edge of the density depression coincides with a transition from southward to northward convection and that the wave power is strongly enhanced inside the depression. Conversely, when zero epoch is chosen to coincide with the V_{nor} reversal (Figures 4f–4j), the density minimum at zero epoch is somewhat less pronounced but still present (Figure 4f). Interestingly, it is preceded by another density minimum observed between –7 and –3 h in the SEA data. The V_{nor} transition is much clearer here, as expected. The wave power is also enhanced inside the depression, in this case between –7

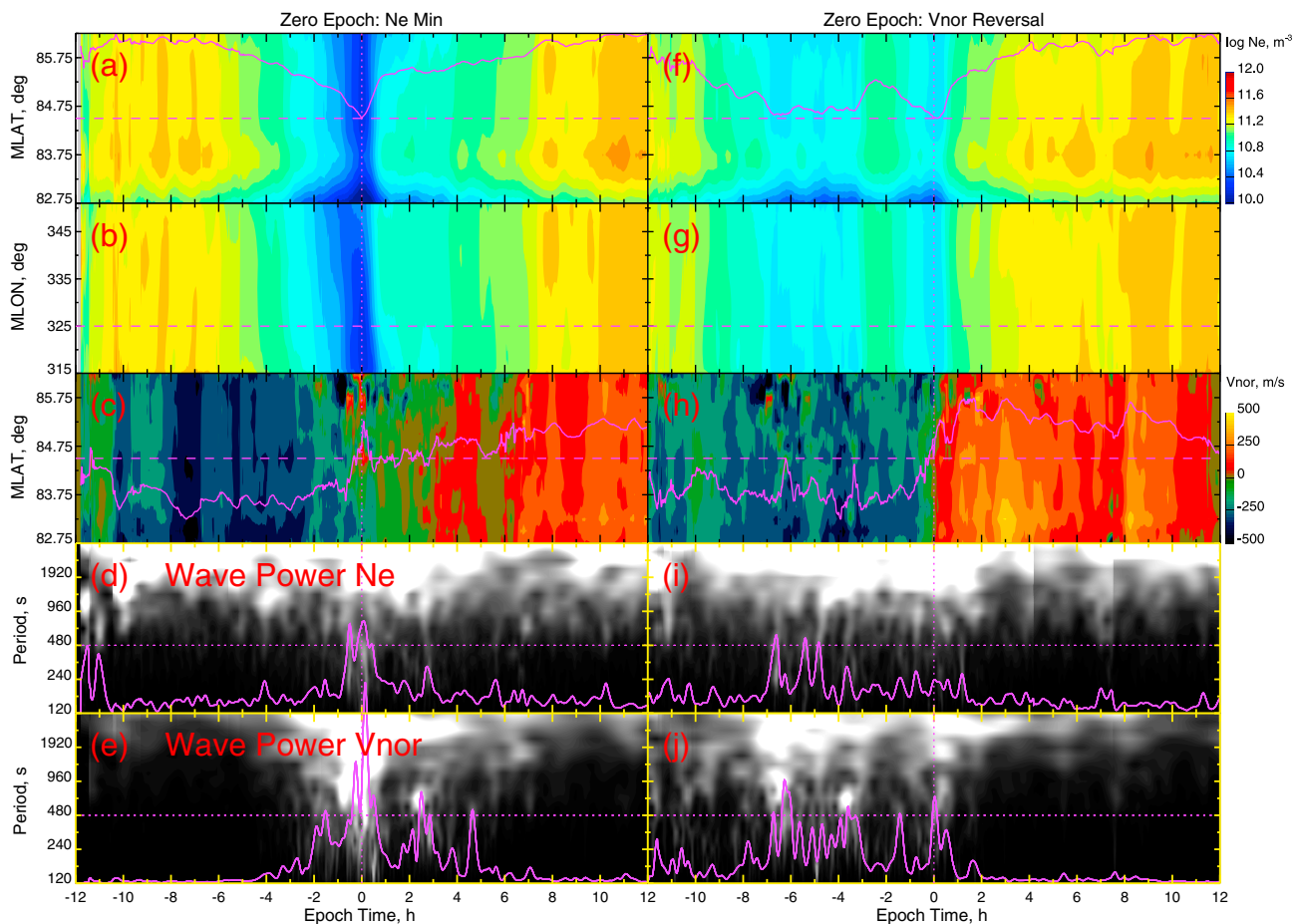


Figure 4. Superposed epoch analysis (SEA) results for (a) NS keogram of electron density, (b) EW keogram of electron density, (c) keogram of NS convection velocity component V_{nor} , (d) wave power of electron density at 325°E , 84.5°N (geomagnetic), and (e) wave power of the convection component V_{nor} . The SEA for the wave power is shown in an arbitrary grey scale, with lighter shades representing higher wave powers. The zero epoch time is the main minimum of the electron density. The pink solid lines show line plots of the respective parameters in an arbitrary scale at a location shown by the pink dashed line in each panel. This line is not given in Figure 4b since it is the same as in Figure 4a. (f–j) The same but with zero epoch time being the reversal of the convection component V_{nor} .

and +1 h (Figures 4i and 4j). Overall, this second SEA confirms the results of the first one, while also revealing a new feature in the form of a double minimum that was often present in the density depressions. Going back to the two examples presented in Figure 3, these may be regarded as representative examples of double-dip (Figures 3a–3e) and single-dip (Figures 3f–3j) depressions.

3.3. Structure Extent and Shape

In this part of the analysis we examine the extent and shape of the density structures observed by RISR-N in the vicinity of density depressions. This was done by considering the lowest-density contour from 2-D density images that was entirely within the MLON/MLAT limits of the image. In this way, the strongest part of the structure is captured in its entirety, and the shape of the contour enclosing this strongest part is assumed to be similar to that for the entire structure. The lower limits on the MLON and MLAT extents of the structure were then estimated from this contour (maximum minus minimum MLON or MLAT of the contour), along with their ratio. Figure 5 presents the results of this analysis for all identified structures. It shows scatterplots of (a) lowest density and (b) ratio of MLON extent to MLAT extent versus UT. In addition, it shows MLAT extent versus MLON extent for (c) all and (d) low-density structures ($\log N_e < 10.6 \text{ m}^{-3}$). The black circles and bars show the binned data, while color coding is in density, with the scale obvious from Figure 5a.

The uncertainties in all shown parameters were estimated by considering the uncertainty in the density measured in the closest RISR-N beam to the structure center, considering the contour at the density perturbed by this uncertainty, computing all parameters at this new perturbed contour, and evaluating all uncertainties as half differences between unperturbed and perturbed values. These individual uncertainties are not shown

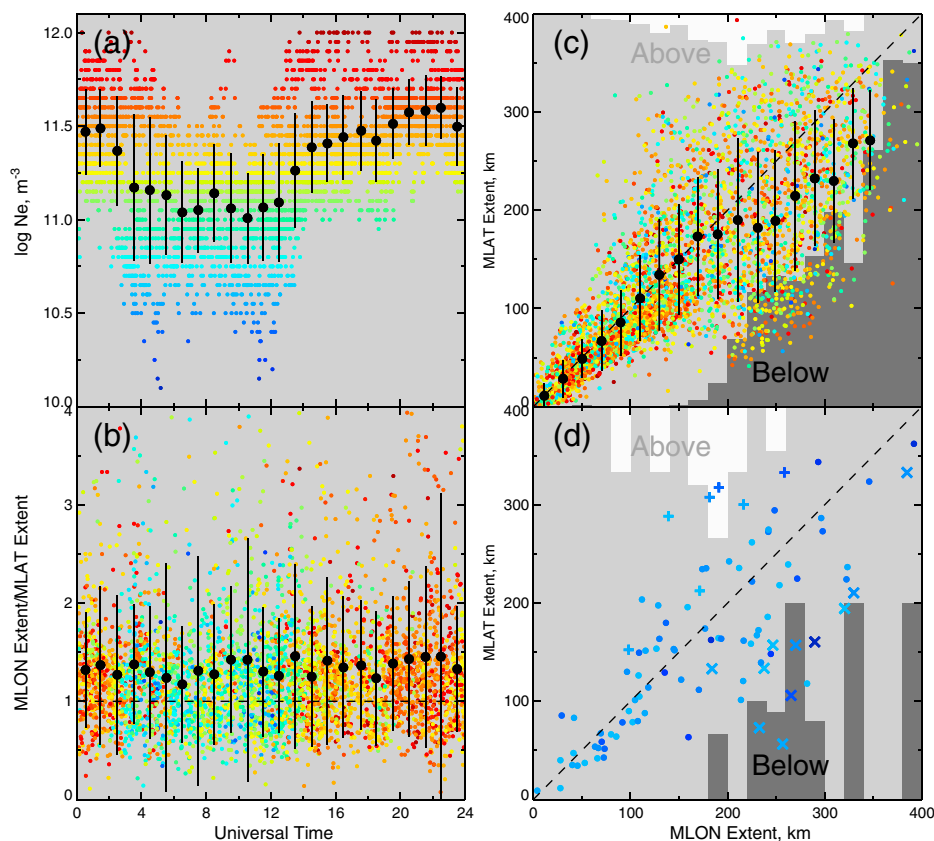


Figure 5. (a) The lowest electron density and (b) the ratio of MLON extent to MLAT extent of the identified density structures versus UT. The MLAT extent versus MLON extent for (c) all identified structures and (d) structures with low density ($\log N_e < 10.6 \text{ m}^{-3}$). The points are color coded in N_e with the scale evident from Figure 5a. The binned data are shown by the black circles and bars in Figures 5a–5c. The light (dark) grey histograms in Figures 5c and 5d show the fraction of individual points that were above (below) the dashed line of ideal coincidence within uncertainty. These points are also shown by pluses (above the line) and crosses (below) in Figure 5d. The scale for histograms is such that 100% is at the top (bottom) for bars starting at the bottom (top).

in Figure 5 to keep the diagram readable, but they were considered in the extent comparisons presented in Figures 5c and 5d, as described later.

Figure 5a shows a familiar double-dip depression feature, with the lowest densities observed near 05 and 12 UT. This is obvious from both individual (blue) points and binned (black) data. No significant change in the ratio is observed inside the depression as evident from both individual points and binned data at 04–12 UT in Figure 5b. This implies that the structures are not much different inside and outside the depression, at least in terms of ratio of extents. On average, the ratio is slightly above 1 in all time sectors, including inside the depressions. This implies that, on average, the structures are slightly more elongated in the EW direction in all MLT sectors, although this is not conclusive since none of the MLT bins have ratio above 1 within uncertainty.

The direct, point-by-point comparison of MLAT and MLON extents shows a somewhat different picture, however (Figures 5c and 5d): namely, in Figure 5c the points below 150 km in MLON extent cluster quite close to the ideal coincidence line. The average binned data (black circles) in particular are located right on the ideal coincidence line, and standard deviations in these values (black bars) are low. Above 150 km, however, the trend changes. Scatter in individual points becomes more significant, and the binned data on average are below the ideal coincidence. At the three largest bins with significant number of points (>10 shown) the binned data are below the ideal coincidence within uncertainty. The fraction of individual points that were below (above) the ideal coincidence line within uncertainty is shown by the dark (light) grey histogram in Figure 5c. In this presentation, 100% is at the top (bottom) for dark (light) bars and the vertical distance between the dark and light bars represents a fraction of individual points that were on the ideal coincidence line within uncertainty. For example, 90% points with MLON extents above 350 km were below the line, with no points above and

10% on the line within uncertainty. This presentation shows that the number of individual points below the ideal coincidence line within uncertainty progressively increases with size increasing, while the number of points above is small.

The above features imply that small-scale structures (<150 km) are mostly circular in shape, while larger structures (>150 km) are more elongated in the EW direction (ratio of MLAT extent to MLON extent <1). Considering now only low-density structures (Figure 5d), one can see that the same features are present here as well. There are more EW elongated structures at large sizes (crosses and dark gray histogram). Thus, there appear to be no substantial differences between low-density structures ($\log N_e < 10.6 \text{ m}^{-3}$) and their high-density counterparts ($\log N_e > 10.6 \text{ m}^{-3}$) in terms of their shapes.

3.4. Structure Propagation and Convection Velocities

The relationship between the structure propagation velocity, plasma velocity, and structure elongation is investigated next. Here we focus on the horizontal component \mathbf{V}_{str} derived from 2-D density images and its comparisons with the plasma drifts \mathbf{V}_{ExB} . Automatic structure identification, tracking, and inferring velocities from series of 2-D images has an advantage of producing true 2-D velocities for most structure shapes. However, this is a nontrivial image analysis problem, with existing solutions limited to a particular imaging system and a particular set of conditions [Makarevitch et al., 2004; Hosokawa et al., 2009; Burston et al., 2014]. In most studies that consider structure velocity, a simpler process is employed in which 1-D or 2-D velocities are inferred from the slope(s) of the linear fit to the consecutive positions of the measured parameter such as density or radar power [e.g., Bahcivan et al., 2010; Oksavik et al., 2010]. In the current study, we employ a similar approach with corrections for apparent motion effect applied based on the set of expressions derived in Appendix 1.

Figure 6 presents the structure propagation analysis for one selected event on 13 October 2012. During this event, plasma convection was strong and reasonably uniform (Figure 3h), a condition under which the \mathbf{V}_{ExB} estimates are of good quality [Heinselman and Nicolls, 2008]. The first two panels show (a) the EW keogram of N_e and (b) the line plot of V_{east} at 84.5° MLAT. A similar plot for V_{nor} is not presented here for brevity. Nine propagating density structures that were clearly visible in both the EW and NS keograms were found; these are highlighted with the dotted lines and digits at the top of Figure 6a. Their apparent velocities in the EW and NS directions (V_{ax} and V_{ay}) were then estimated from the slopes of the manually selected fit lines. These fit lines are shown by dotted lines in Figure 6a and used to find V_{ax} . The derived estimates for V_{ax} are shown by the red circles and bars in Figure 6b. The V_{ax} and V_{ay} estimates were then converted into the corrected structure velocity \mathbf{V}_c using equation (A8). These estimates for the V_{cx} component are shown by the blue circles and bars in Figure 6b. In addition, Figure 6b presents by the digits at the top of Figure 6b the inferred structure elongation slope k from equation (A5) and the angle δ between the corrected and drift velocities from Equation (A9).

In estimating angles δ we used estimates of \mathbf{V}_c and \mathbf{V}_d under the assumption that $\mathbf{V}_d = \mathbf{V}_{\text{ExB}}$. The \mathbf{V}_d estimates were taken from convection velocities \mathbf{V}_{ExB} averaged over the time interval when each individual structure was within the RISR-N FoV (horizontal span of each dotted line in Figure 6a). These were also compared with the apparent and corrected velocities in Figures 6c–6f. The scatterplots of the apparent velocity versus convection velocity are presented in Figures 6c and 6d in terms of their x and y components, respectively, while the same analysis for corrected velocity is presented in Figures 6e and 6f.

Finally, Figures 6g–6j present 2-D density images for four selected structures, along with the convection (black) and corrected (blue) velocity vectors. As described in section 2, the convection vectors are available in 0.25° bins in MLAT and these are assigned to a MLON of 325° E in the current study. The corrected velocity, on the other hand, is only available at one point corresponding to the MLAT and MLON of the selected keograms.

From Figures 6b–6f, the corrected structure velocity agrees with the convection velocity within uncertainty. For example, all blue points in Figures 6e and 6f are on the dashed line of ideal coincidence within uncertainty, while in Figures 6c and 6d only a few red points are close to this line. The agreement between the corrected and convection velocities is also clear from the 2-D presentation of Figures 6g–6j, where the blue vector is of approximately the same length and direction as the black vectors nearby. One should reiterate here that the exact agreement is expected only if structures drift with \mathbf{V}_{ExB} and in a direction perpendicular to their elongation, i.e., when $\delta = 0$. In this context, Figure 6 shows that this is approximately the case, with δ estimates being below 24° and with black and blue vectors being roughly perpendicular to most contours in Figures 6g–6j.

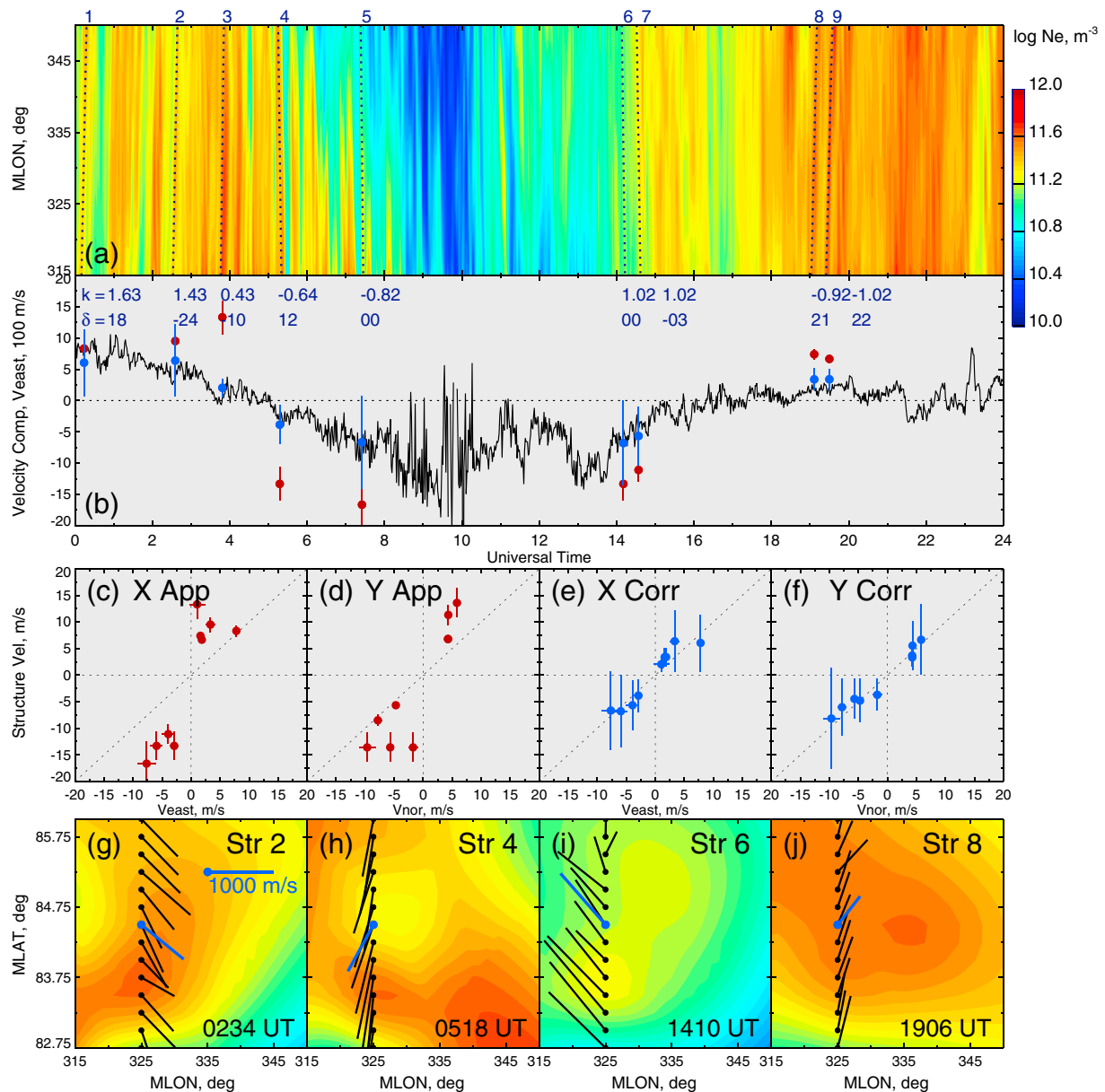


Figure 6. (a) EW keogram of electron density for 13 October 2012. Nine selected propagating structures are shown by the dotted lines and digits at the top. (b) EW convection velocity component at 84.5°N MLAT. The apparent (corrected) velocity EW component for nine individual structures is shown by the red (blue) circles. The structure elongation slope k and the inferred angle between the corrected and convection velocity δ (in degrees) are shown by the digits at the top of Figure 6b. The apparent structure velocity (c) EW and (d) NS component versus the respective ion velocity component. (e and f) The same as Figures 6c and 6d but for corrected structure velocity. (g–j) Two-dimensional images of four selected structures. The corrected structure (convection) velocities are shown by blue (black) vectors.

Overall, this analysis supports the notion that density structures drift with the plasma convection and that their elongation direction is roughly perpendicular to the drift direction.

4. Discussion

In this study, propagating plasma structures in the vicinity of polar holes were investigated using a new-generation ISR system in Resolute Bay, Canada (RISR-N). The multipoint nature of RISR-N observations and short cadence intervals allowed us to further investigate highly dynamic plasma structuring processes in the polar cap with minimal spatiotemporal ambiguities. The important new aspect of this study was its focus on continuous and multipoint radar observations of deep plasma density depressions in the polar cap. Pre-

viously, these have been predominantly studied using data sets accumulated over multiple satellite passes complemented by single-point ground-based observations [Brinton *et al.*, 1978; Hoegy and Grebowsky, 1991; Doe *et al.*, 1993; Benson and Grebowsky, 2001]. Investigations of density depressions can be regarded as a complementary effort to studies of production and evolution of plasma enhancements such as polar patches [Crowley *et al.*, 1993]. In this sense, the current study complements well the recent experimental studies of polar patches that were enabled by expanding capabilities to image the polar cap using radio and optical techniques [e.g., Hosokawa *et al.*, 2009, 2014; Oksavik *et al.*, 2010; Dahlgren *et al.*, 2012b; Moen *et al.*, 2013; Zhang *et al.*, 2013; Burston *et al.*, 2014; Nishimura *et al.*, 2014]. Moreover, the current study also focused on series of propagating density enhancements in the vicinity of density depressions and can therefore be regarded as complementary to both of these broader efforts. In the rest of this section, we further discuss three groups of issues aligned with the objectives of this study.

4.1. Density Depressions: Characteristics and Relation to Plasma Convection

All density measurements were considered near an altitude of 300 km, since this was the altitude considered in initial studies of polar holes [Brinton *et al.*, 1978; Hoegy and Grebowsky, 1991] and since the RISR-N footprint at this altitude was well sampled by 11 beams, i.e., with relatively small separations between beam footprints and similar separations/extents in MLON and MLAT (Figure 1).

Density depressions were identified within the RISR-N data set as events that had at least 1% of measurements with $N_e < 4 \times 10^{10} \text{ m}^{-3}$ and at least 10% of measurements with $N_e < 10^{11} \text{ m}^{-3}$. While these density limits may seem somewhat high as compared with some previous studies of polar holes (see section 1), one should bear in mind the following considerations. First, at the typical MLATs of RISR-N observations near 85°N density depletions are not as deep as the deepest polar holes reported at 70°–80° [Brinton *et al.*, 1978]. Second, the period under investigation was not at the exact solar minimum (in 2009–2010), so higher densities are expected, including inside the deepest polar holes. A look into RISR-N densities from the 2009–2011 winter seasons indicate that the densities were indeed lower and more in line with the lowest density of $2 \times 10^8 \text{ m}^{-3}$ reported previously (not presented here). The reason why this later period was selected for investigation was a significant presence of small-scale and mesoscale density structures in the vicinity of low-density regions, which was another focus of this study. Moreover, the presence of low-density regions with $N_e < 4 \times 10^{10} \text{ m}^{-3}$ on an ascending phase and even near the peak of a weak solar cycle also deserves some attention. In view of the above, the current observations refer to either a poleward extension of the polar hole region “proper” and/or a weaker version of polar holes considered in the past.

A comparison with the expected trends as represented by the IRI model (Figure 2) showed that the observed density behavior inside the depressions did not have a clear accompanying signature in the model output. Since all events of interest were selected based on their low densities, this result by itself is not that significant. However, what was more significant and unexpected was the fact that RISR-N densities were generally low throughout the winter season (grey line and stripe in Figure 2). For example, the IRI trends for winter were at the top of this normal winter range around 10 UT; the hourly means were comparable between the all-winter and depressions-only data sets (grey line and blue circles, respectively, in Figure 2), and both were lower, on average, than IRI trends. On the one hand, this is consistent with poorer agreement between modeled and measured densities during periods not dominated by the solar, locally produced ionization [Themens *et al.*, 2014]. On the other hand, the same study by Themens *et al.* [2014] demonstrated that IRI densities tend to be lower during winter than those measured by the Canadian Advanced Digital Ionosonde (CADI) (see their Figure 2). Considering that RISR-N densities are normally calibrated using the CADI at Resolute Bay during nighttime and winter conditions, the same is expected for the IRI-RISR comparisons, i.e., lower model densities, while in our study model densities were higher. The disagreement may be due to different solar cycle phases (2008–2010 near solar minimum in Themens *et al.* [2014] versus our 2012–2013 near a weak solar maximum) and higher occurrence of polar holes in our observations as compared with what is predicted by IRI.

The low plasma densities measured by RISR-N in the winter nighttime ionosphere also prompt a discussion of quality of RISR-N measurements under these conditions. As described in section 2, fractional uncertainties in the plasma density $\Delta N_e/N_e$ depend on several parameters and are typically below 10% in the ISR technique. Ionospheric densities in the broad range are observed by ISRs including those in the polar hole region [Robinson, 1991; Doe *et al.*, 1993; Pedersen *et al.*, 1998]. Individual uncertainties representative of the densities analyzed in the current study were given in Figure 2. The fractional uncertainties were significantly larger at $N_e < 4 \times 10^{10} \text{ m}^{-3}$ or at $\log N_e < 10.6$ (see longer green lines in Figure 2a), but even at these low densities

the uncertainties did not increase to the point of making measurements unusable. Thus, for black points below $\log N_e = 10.25$ near 5 UT and 12 UT in Figure 2a, the green lines did not extend above $\log N_e = 10.5$, which means that the density depressions were real and significant. At higher densities of $N_e > 10^{11} \text{ m}^{-3}$ observed inside density enhancements, which was another focus of the current study, the individual density uncertainties were all smaller than 10% (Figure 2).

Information about plasma convection is critical in assessing the role of plasma transport in polar hole formation and evolution. This is because polar holes are assumed to be formed when convection is either very slow [Brinton *et al.*, 1978; Sojka *et al.*, 1981a, 1981b] or perhaps strongly enhanced [Sojka *et al.*, 1981c]. In most previous experimental investigations of polar holes, however, the convection context was mainly provided by statistical maps [Brinton *et al.*, 1978; Benson and Grebowsky, 2001] since concurrent measurements were not available. A notable exception is the study by Doe *et al.* [1993] that considered LOS convection component measurements by an ISR system at Sondrestrom near 00 MLT, which provided evidence of a convection shear near an auroral cavity. The current study takes one step forward in establishing the role of plasma convection by considering simultaneous and concurrent convection measurements by RISR-N.

The superposed epoch analysis conducted for plasma density and zonal convection component showed that the main density minimum was associated with a change in convection from predominately equatorward $V_{\text{nor}} < 0$ to near zero $V_{\text{nor}} \approx 0$ and then to predominately poleward $V_{\text{nor}} > 0$ (Figures 4a–4c). For the SEA with zero epoch at the V_{nor} reversal, a converse result was observed, i.e., the density had a minimum at zero epoch (Figures 4f–4h), although in this case it was less deep and preceded by a secondary density peak and another more extended minimum before that.

The differences in results using two analyses (Figures 4a–4d and 4f–4h) are a consequence of this double-dip feature of the depressions observed for several events, e.g., 20130212 in Figure 2 or 20121008 in Figure 3a. In other cases, a single-minimum depression was observed, e.g., 20121013 in Figure 3f. We believe that this double-dip feature is related to the small-scale variability, which is further discussed in the next section. In terms of convection, the following generalization can be made for both cases. Density depressions well inside the polar cap (MLATs near 85°N) have a minimum just before convection changes from equatorward to poleward. Such a transition occurs in the dawn sector near 06 MLT at the most equatorward point of the streamlines. This is generally consistent with previous studies that also place polar holes in the dawn sector [Brinton *et al.*, 1978]. A new result is that a density minimum (either the primary or a secondary) occurs deep inside the dawn sector and in many cases just before or perhaps even slightly after 06 MLT. This fits well with the idea of an extended polar hole to which the current observations probably refer.

This prompts the question, however, of whether a sharp density increase at this point is simply due to an increased solar illumination near sunrise which quickly wipes out the polar hole. This does not appear to be the case since the timing, shapes, and rates of the measured increases were different from those seen in the IRI density (Figure 3) and since IRI reproduces changes due to solar illumination particularly well. Thus, an increase in the IRI density is monotonic and particularly strong near 11 UT in Figures 2 and 3, while the measured increases had plateaus and often did not have a clear “main” rise. In addition, for double-dip events, a strong density increase is observed after the first minimum and this is too early to be due to a sunrise.

4.2. Density Perturbations in the Vicinity of Density Depressions

In this study, strong fluctuations in both the plasma density and the convection velocity were found within the polar hole region. The wave power from the wavelet analysis had a peak near the depression minimum (Figures 4d and 4e). In addition, series of propagating density enhancements were seen in some events during the same intervals that were occupied by density depressions in other events and on the background of relatively low densities (Figures 3a and 3d). While similar density enhancements were seen in all time sectors, they were the strongest relative to the background inside depressions (Figure 4). Moreover, these series were strong enough to significantly raise overall density level to be more comparable with the daytime densities. This was also seen as a secondary maximum inside the depressions for several events (Figures 2a and 3a), which was also reflected in the SEA results (Figure 4f).

This prompts the question of whether strong density perturbations can, fully or in part, refill polar holes and whether these enhancements are local or transported from the outside. Perturbation densities comparable with daytime values suggest the latter. Certainly, series of polar patches formed in the dayside ionosphere and transported toward the nightside with the plasma convection would have these properties. It is not entirely

clear, however, why the same recombination processes that were probably responsible for density depletions did not affect much polar patches entering and propagating through the polar hole. Long cross-polar-cap drift times of several hours and the associated slow convection of <0.1 km/s are thought to be enough to cause deep plasma depressions inside polar holes [Brinton *et al.*, 1978]. The fact that the density inside the enhancements was comparable to daytime values implies that their propagation was not particularly slow throughout the entire trip across the polar cap, which matches well with their considerable velocities in the final stages of this transport process (Figure 6). The other explanation involves nonuniform polar cap convection, with faster flows forming a channel around polar patches and slower background flows in the polar hole. Such channels are well documented in observations near the cusp region [Carlson *et al.*, 2002], and the current observations suggest that these may persist all the way to the dawn sector. Polar patches exit the polar cap in a wide range of MLT, with some as late as 04 MLT [Moen *et al.*, 2007], and the current study suggests that polar patches can pass through most of the polar cap without dissipating even in its significantly depleted state.

4.3. Density Structure Shapes and Propagation

In this study, we also addressed the issue about relationship between the structure velocity, structure shape, and background convection (section 3.4). The structure shapes were found to be mostly circular at small scales (<150 km) but more elongated in the EW direction at larger scales (Figure 5). The latter statistical result is consistent with recent observations by Hosokawa *et al.* [2014] for one case event and predictions by Carlson [2003] that most structures should be cigar shaped rather than circular if they were to form by transient magnetic reconnection [Lockwood and Carlson, 1992]. The former result implies, on the other hand, that small-scale structures are different in their characteristics and generation mechanisms. One candidate formation mechanism is through particle precipitation (see the recent paper by Goodwin *et al.* [2015, and references therein]), with the current observations indicating that characteristic scales produced are below 150 km.

In propagation analysis, an agreement within uncertainty was found between the structure propagation velocity \mathbf{V}_c and the plasma convection velocity $\mathbf{V}_{E \times B}$ (Figure 6). The former was inferred from EW and NS density keograms with corrections for apparent motion taken into account, while the latter was determined from direct ion velocity measurements by RISR-N. Qualitatively, structures were also propagating in a direction consistent with $\mathbf{V}_{E \times B}$ (Figures 3d, 3e, 3i, and 3j). Importantly, while this agreement is expected for polar patches that propagate deep within the polar cap, questions remain as to what happens on entry and exit, i.e., in the vicinity of reconnection regions where the magnetic tension force is a significant factor [Carlson, 2012]. In addition, experimental comparisons to date have been mostly qualitative and/or with significant involvement of statistical convection models and particle tracing techniques [Moen *et al.*, 2007; Oksavik *et al.*, 2010]. In this context, an interesting result of the current study is that the velocity agreement was observed in all time sectors including near 00 MLT (07 UT) (Figures 3 and 6). In addition, no evidence of faster convection within the structures was obtained (Figures 6g–6j). A useful extension of the current analysis would be the development of an automatic algorithm for structure tracking and velocity estimates using ISR data. As discussed in sections 1 and 3.4, this presents numerous challenges including the need to apply corrections if measurements in EW-aligned and NS-aligned sampling areas are considered or the need to appropriately characterize individual structures if 2-D images are used [e.g., Makarevitch *et al.*, 2004; Dahlgren *et al.*, 2012a; Burston *et al.*, 2014].

5. Summary and Conclusions

The statistical analysis of the Resolute Bay Incoherent Scatter Radar observations in the winter polar cap F region shows the following:

1. Significant density depressions occur near the peak of a weak solar cycle and poleward of the previously identified polar hole-auroral cavity region. They exhibit a single-dip or double-dip temporal variation, with the primary or secondary (if present) minimum coinciding with the plasma convection reversal from the equatorward to poleward flow. Density depressions can form under a variety of convection conditions, without strong preference toward either slow or fast convection.
2. The winter polar cap is also characterized by multiple series of propagating density enhancements present in both the density and convection data. The spatial scales of density enhancements range between 50 and 400 km (maximum extent imaged by RISR-N at 300 km altitude). The density enhancements are quasiperiodic, and enhanced wave power is seen both well outside and in the vicinity of density depressions. In the case of a double-dip depression, the wave power peaks near the density minimum. The density

enhancements are strong enough to be a significant source for refilling of density depressions, and their origin is likely to be polar patches of dayside plasma convecting antisunward across the polar cap.

3. The density enhancements are mostly circular in shape at small scales (<150 km) but more elongated in the zonal direction at larger scales. The latter finding is consistent with polar patches being stretched in the zonal direction by the magnetic tension force in the course of quasiperiodic magnetic reconnection. The small-scale structures are more likely to be formed by particle precipitation. The propagation analysis is consistent with structures drifting with background plasma in a direction perpendicular to their elongation in all time sectors. This means that the magnetic tension force is no longer a factor by the time the structures are deep within the polar cap, regardless of their prior history.

Appendix A: Apparent and Corrected Structure Velocities

Let us consider an elongated structure with a slope $k = \tan \gamma$, where γ is the angle the structure makes with the x axis (Figure A1). If measurements of the structure position are only conducted on the x and y axes (e.g., EW and NS keograms or stackplots produced from measurements in beams that are aligned zonally and meridionally, respectively), then the propagation analysis proceeds as follows. A structure drifting with a true horizontal velocity \mathbf{V}_d can be described parametrically as

$$\mathbf{r}(t) = s \cos \gamma \hat{\mathbf{e}}_x + s \sin \gamma \hat{\mathbf{e}}_y + \mathbf{V}_d t, \tag{A1}$$

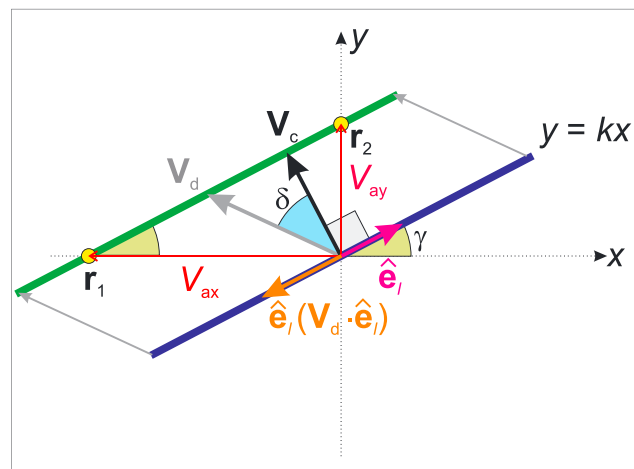
where parameter s takes values in the range $[-a, a]$ and a is the structure half-length.

The apparent structure velocities V_{ax} and V_{ay} that will be measured in this geometry are those of the points $\mathbf{r}_1(t) = (x_1(t), 0)$ and $\mathbf{r}_2(t) = (0, y_2(t))$ at the intersection of the structure with the x and y axes, respectively (Figure A1). From equation (A1),

$$x_1(t) = s_1 \cos \gamma + V_{dx} t = V_{ax} t, \quad y_1(t) = s_1 \sin \gamma + V_{dy} t = 0,$$

$$x_2(t) = s_2 \cos \gamma + V_{dx} t = 0, \quad y_2(t) = s_2 \sin \gamma + V_{dy} t = V_{ay} t. \tag{A2}$$

The apparent velocities can be expressed from equation (A2) by eliminating s_1 and s_2



$$V_{ax} = -V_{dy} \cot \gamma + V_{dx} = -V_{dy}/k + V_{dx}, \tag{A3}$$

$$V_{ay} = -V_{dx} \tan \gamma + V_{dy} = -V_{dx}k + V_{dy}. \tag{A4}$$

From multiplying equation (A3) by k and adding with equation (A4), $V_{ax}k + V_{ay} = 0$, and the final expression for the elongation slope is

$$k = -\frac{V_{ay}}{V_{ax}}. \tag{A5}$$

Figure A1. Geometry of observations showing an elongated structure with a slope $k = \tan \gamma$. The structure drifts with a velocity \mathbf{V}_d (grey vectors), while measurements are conducted on the x and y axes, and motions of the two intersection points \mathbf{r}_1 and \mathbf{r}_2 (yellow) are tracked. The red vectors show apparent velocities V_{ax} and V_{ay} corresponding to these points. Also shown are the unit vector along elongation direction $\hat{\mathbf{e}}_l$ (pink), the elongation-parallel drift velocity $\hat{\mathbf{e}}_l (\mathbf{V}_d \cdot \hat{\mathbf{e}}_l)$ (orange), and the elongation-perpendicular velocity \mathbf{V}_c (black).

Figure A1 shows that the drift velocity \mathbf{V}_d can be decomposed into components perpendicular and parallel to the structure elongation and that only the former can be determined from the apparent velocity measurements: namely,

$\mathbf{V}_d = \mathbf{V}_c + \hat{\mathbf{e}}_l (\mathbf{V}_d \cdot \hat{\mathbf{e}}_l)$, where \mathbf{V}_c is the perpendicular component (which is also the corrected velocity that we need to find) and $\hat{\mathbf{e}}_l$ is the unit vector along the structure. From Figure A1, it is also easy to see that

$$\hat{\mathbf{e}}_l = \cos \gamma \hat{\mathbf{e}}_x + \sin \gamma \hat{\mathbf{e}}_y = \cos \arctan k \hat{\mathbf{e}}_x + \sin \arctan k \hat{\mathbf{e}}_y = \frac{\hat{\mathbf{e}}_x + k \hat{\mathbf{e}}_y}{\sqrt{1 + k^2}} \quad (\text{A6})$$

and that

$$\mathbf{V}_c = V_{ax} \hat{\mathbf{e}}_x - V_{ax} \cos \gamma \hat{\mathbf{e}}_l = V_{ax} \hat{\mathbf{e}}_x - \frac{V_{ax} \hat{\mathbf{e}}_l}{\sqrt{1 + k^2}}. \quad (\text{A7})$$

The final expression for the corrected velocity is obtained by substituting the unit vector $\hat{\mathbf{e}}_l$ from equation (A6), substituting the slope k from equation (A5), and simplifying

$$\mathbf{V}_c = \frac{V_{ax} V_{ay}^2 \hat{\mathbf{e}}_x + V_{ay} V_{ax}^2 \hat{\mathbf{e}}_y}{V_{ax}^2 + V_{ay}^2}. \quad (\text{A8})$$

This expression is nicely symmetric and valid for all possible apparent velocities V_{ax} and V_{ay} . If both of these quantities are known, the elongation slope k and the corrected structure velocity \mathbf{V}_c can be found from equations (A5) and (A8), respectively. In addition, if the true drift velocity \mathbf{V}_d is known, the angle between the elongation direction and the drift velocity can be found or, equivalently, a complementary angle δ between \mathbf{V}_c and \mathbf{V}_d

$$\delta = \cos^{-1} \frac{\mathbf{V}_d \cdot \mathbf{V}_c}{V_d V_c}. \quad (\text{A9})$$

Acknowledgments

This work was supported by NSF grant AGS-1248127. The Resolute Bay Incoherent Scatter Radar North is operated by SRI International on behalf of the US National Science Foundation under NSF Cooperative Agreement AGS-1133009. The data are accessible from the SRI International online database at <http://amisr.sri.com/database/>. The IRI model code is available at <http://irimodel.org/>.

Alan Rodger thanks two reviewers for their assistance in evaluating this paper.

References

- Bahcivan, H., R. Tsunoda, M. Nicolls, and C. Heinselman (2010), Initial ionospheric observations made by the new Resolute Incoherent Scatter Radar and comparison to solar wind IMF, *Geophys. Res. Lett.*, *37*, L15103, doi:10.1029/2010GL043632.
- Benson, R. F., and J. M. Grebowsky (2001), Extremely low ionospheric peak altitudes in the polar hole region, *Radio Sci.*, *36*, 277–285, doi:10.1029/1999RS002401.
- Bilitza, D., and B. W. Reinisch (2008), International reference ionosphere 2007: Improvements and new parameters, *Adv. Space Res.*, *42*, 599–609, doi:10.1016/j.asr.2007.07.048.
- Brinton, H. C., J. M. Grebowsky, and L. H. Brace (1978), The high-latitude winter *F* region at 300 km—Thermal plasma observations from AE-C, *Geophys. Res. Lett.*, *5*, 4767–4776.
- Buchau, J., B. W. Reinisch, E. J. Weber, and J. G. Moore (1983), Structure and dynamics of the winter polar cap *F* region, *Radio Sci.*, *18*, 995–1010.
- Burston, R., K. Hodges, I. Astin, and P. T. Jayachandran (2014), Automated identification and tracking of polar-cap plasma patches at solar minimum, *Ann. Geophys.*, *32*, 197–206, doi:10.5194/angeo-32-197-2014.
- Carlson, H. C. (2003), A voyage of discovery into the polar cap and Svalbard, in *Proceedings of the Egeland Symposium on Auroral and Atmospheric Research*, edited by J. Moen and J. A. Holtet, pp. 33–54, Dept. of Phys., Univ. of Oslo, Norway.
- Carlson, H. C. (2012), Sharpening our thinking about polar cap ionospheric patch morphology, research, and mitigation techniques, *Radio Sci.*, *47*, RS0L21, doi:10.1029/2011RS004946.
- Carlson, H. C., K. Oksavik, J. Moen, A. P. van Eyken, and P. Guio (2002), ESR mapping of polar-cap patches in the dark cusp, *Geophys. Res. Lett.*, *29*(10), 1386, doi:10.1029/2001GL014087.
- Carlson, H. C., T. Pedersen, S. Basu, M. Keskinen, and J. Moen (2007), Case for a new process, not mechanism, for cusp irregularity production, *J. Geophys. Res.*, *112*, A11304, doi:10.1029/2007JA012384.
- Crowley, G., H. C. Carlson, S. Basu, W. F. Denig, J. Buchau, and B. W. Reinisch (1993), The dynamic ionospheric polar hole, *Radio Sci.*, *28*, 401–413.
- Dahlgren, H., G. W. Perry, J. L. Semeter, J.-P. St.-Maurice, K. Hosokawa, M. J. Nicolls, M. Greffen, K. Shiokawa, and C. Heinselman (2012a), Space-time variability of polar cap patches: Direct evidence for internal plasma structuring, *J. Geophys. Res.*, *117*, A09312, doi:10.1029/2012JA017961.
- Dahlgren, H., J. L. Semeter, K. Hosokawa, M. J. Nicolls, T. W. Butler, M. G. Johnsen, K. Shiokawa, and C. Heinselman (2012b), Direct three-dimensional imaging of polar ionospheric structures with the Resolute Bay Incoherent Scatter Radar, *Geophys. Res. Lett.*, *39*, L05104, doi:10.1029/2012GL050895.
- Davis, C., and I. McCrea (2004), Estimating uncertainties in incoherent scatter radar parameters from random variations in time series data, *Ann. Geophys.*, *22*, 3523–3529, doi:10.5194/angeo-22-3523-2004.
- Doe, R. A., M. Mendillo, J. F. Vickrey, L. J. Zanetti, and R. W. Eastes (1993), Observations of nightside auroral cavities, *Geophys. Res. Lett.*, *20*, 293–310.
- Evans, J. V. (1969), Theory and practice of ionosphere study by Thomson Scatter Radar, *Proc. IEEE*, *57*, 496–530.
- Goodwin, L. V., et al. (2015), Swarm in situ observations of *F* region polar cap patches created by cusp precipitation, *Geophys. Res. Lett.*, *42*, 996–1003, doi:10.1002/2014GL026210.
- Heinselman, C. J., and M. J. Nicolls (2008), A Bayesian approach to electric field and *E*-region neutral wind estimation with the Poker Flat Advanced Modular Incoherent Scatter Radar, *Radio Sci.*, *43*, RS5013, doi:10.1029/2007RS003805.

- Hoegy, W. R., and J. M. Grebowsky (1991), Dependence of polar hole density on magnetic and solar conditions, *Geophys. Res. Lett.*, *96*, 5737–5755.
- Hosokawa, K., T. Kashimoto, S. Suzuki, K. Shiokawa, Y. Otsuka, and T. Ogawa (2009), Motion of polar cap patches: A statistical study with all-sky airglow imager at Resolute Bay, Canada, *J. Geophys. Res.*, *114*, A04318, doi:10.1029/2008JA014020.
- Hosokawa, K., S. Taguchi, K. Shiokawa, Y. Otsuka, Y. Ogawa, and M. Nicolls (2014), Global imaging of polar cap patches with dual airglow imagers, *Geophys. Res. Lett.*, *41*, 1–6, doi:10.1002/2013GL058748.
- Kellerman, A. C., and R. A. Makarevich (2011), The response of auroral absorption to substorm onset: Superposed epoch and propagation analyses, *J. Geophys. Res.*, *116*, A05312, doi:10.1029/2010JA015972.
- Lockwood, M., and H. C. Carlson Jr. (1992), Production of polar cap electron density patches by transient magnetopause reconnection, *Geophys. Res. Lett.*, *19*, 1731–1734.
- Makarevitch, R. A., F. Honary, I. W. McCrea, and V. S. C. Howells (2004), Imaging riometer observations of drifting absorption patches in the morning sector, *Ann. Geophys.*, *22*, 3461–3478.
- Milan, S. E., M. Lester, and T. K. Yeoman (2002), HF radar polar patch formation revisited: Summer and winter variations in dayside plasma structuring, *Ann. Geophys.*, *20*, 487–499.
- Moen, J., N. Gulbrandsen, D. A. Lorentzen, and H. C. Carlson (2007), On the MLT distribution of *F* region polar cap patches at night, *Geophys. Res. Lett.*, *34*, L14113, doi:10.1029/2007GL029632.
- Moen, J., K. Oksavik, T. Abe, M. Lester, Y. Saito, T. A. Bekkeng, and K. S. Jacobsen (2012), First in situ measurements of HF radar echoing targets, *Geophys. Res. Lett.*, *39*, L07104, doi:10.1029/2012GL051407.
- Moen, J., K. Oksavik, L. Alfonsi, Y. Daabakk, V. Romano, and L. Spogli (2013), Space weather challenges of the polar cap ionosphere, *J. Space Weather Space Clim.*, *3*(26), A02, doi:10.1051/swsc/2013025.
- Nicolls, M. J., C. J. Heinselman, E. A. Hope, S. Ranjan, M. C. Kelley, and J. D. Kelly (2007), Imaging of polar mesosphere summer echoes with the 450 MHz Poker Flat Advanced Modular Incoherent Scatter Radar, *Geophys. Res. Lett.*, *34*, L20102, doi:10.1029/2007GL031476.
- Nishimura, Y., et al. (2014), Day-night coupling by a localized flow channel visualized by polar cap patch propagation, *Geophys. Res. Lett.*, *41*, 3701–3709, doi:10.1002/2014GL060301.
- Oksavik, K., V. L. Barth, J. Moen, and M. Lester (2010), On the entry and transit of high-density plasma across the polar cap, *J. Geophys. Res.*, *115*, A12308, doi:10.1029/2010JA015817.
- Oksavik, K., J. Moen, M. Lester, T. A. Bekkeng, and J. K. Bekkeng (2012), In situ measurements of plasma irregularity growth in the cusp ionosphere, *J. Geophys. Res.*, *117*, A11301, doi:10.1029/2012JA017835.
- Pedersen, T. R., B. G. Fejer, R. A. Doe, and E. J. Weber (1998), Incoherent scatter radar observations of horizontal *F* region plasma structure over Sondrestrom, Greenland, during polar cap patch events, *Radio Sci.*, *33*, 1847–1866, doi:10.1029/98RS01702.
- Rishbeth, H., and P. J. S. Williams (1985), The EISCAT ionospheric radar: The system and its early results, *Q. J. R. Astron. Soc.*, *26*, 478–512.
- Robinson, R. M. (1991), A survey of polar cap *F* region electron densities measured by the Sondrestrom radar, *Radio Sci.*, *26*, 1069–1078, doi:10.1029/91RS00581.
- Rodger, A. S., M. Pinnock, J. R. Dudeney, K. B. Baker, and R. A. Greenwald (1994), A new mechanism for polar patch formation, *J. Geophys. Res.*, *99*, 6425–6436.
- Sojka, J. J., W. J. Raitt, and R. W. Schunk (1981a), A theoretical study of the high-latitude winter *F* region at solar minimum for low magnetic activity, *J. Geophys. Res.*, *86*, 609–621.
- Sojka, J. J., W. J. Raitt, and R. W. Schunk (1981b), Theoretical predictions for ion composition in the high-latitude winter *F*-region for solar minimum and low magnetic activity, *J. Geophys. Res.*, *86*, 2206–2216.
- Sojka, J. J., W. J. Raitt, and R. W. Schunk (1981c), Plasma density features associated with strong convection in the winter high-latitude *F* region, *J. Geophys. Res.*, *86*, 6908–6916.
- Themens, D., P. Jayachandran, M. J. Nicolls, and J. W. MacDougall (2014), A top to bottom evaluation of IRI-2007 within the polar cap, *J. Geophys. Res. Space Physics*, *119*, 6689–6703, doi:10.1002/2014JA020052.
- Weber, E. J., J. Buchau, J. G. Moore, J. R. Sharber, R. C. Livingston, J. D. Winningham, and B. W. Reinisch (1984), *F* layer ionization patches in the polar cap, *J. Geophys. Res.*, *89*, 1683–1694.
- Zhang, Q.-H., M. Lockwood, J. C. Foster, S.-R. Zhang, B.-C. Zhang, I. W. McCrea, J. Moen, M. Lester, and J. M. Ruohoniemi (2015), Direct observations of the full Dungey convection cycle in the polar ionosphere for southward interplanetary magnetic field conditions, *J. Geophys. Res.*, *120*, 4519–4530, doi:10.1002/2015JA021172.
- Zhang, Q.-H., et al. (2013), Direct observations of the evolution of polar cap ionization patches, *Science*, *339*, 1597–1600.